Applied Surface Science 713 (2025) 164339

Contents lists available at ScienceDirect

Applied Surface Science

journal homepage: www.elsevier.com/locate/apsusc

Full Length Article

Activation of NdFeB magnetic material upon exposure to oxygen plasma

Domen Paul [a,b], Alenka Vesel [a], Miran Mozetič [a], Rok Zaplotnik [a], Marian Lehocky [c], Nataša Kovačević [d], Gregor Primc [a,*]

[a] Jozef Stefan Institute, Department of Surface Engineering, Jamova cesta 39, 1000 Ljubljana, Slovenia
[b] Alma Mater Europaea, Slovenska ulica 17, 2000 Maribor, Slovenia
[c] Centre of Polymer Systems, Tomas Bata University in Zlín 76001 Zlín, Czech Republic
[d] Kolektor Mobility d.o.o., SI-5280 Idrija, Slovenia

ARTICLE INFO

Keywords:
Bonded magnets
NdFeB
Wettability
Oxygen plasma
Oxidation
Phase formation

ABSTRACT

In bonded NdFeB magnets, the fillers' adhesion in the polymer matrix of composites is often insufficient, necessitating filler wettability modification before mixing with liquid polymers. Inductively coupled radio-frequency oxygen plasma was used to modify the surface wettability of commercial NdFeB flakes. A pronounced minimum in water contact angle (WCA) was observed after approximately 100 ms of treatment in plasma (50 Pa, 500 W). A deeper minimum was observed upon treatment in the flowing afterglow. The flux of oxygen atoms on the NdFeB flakes' surface was ~3×10^{23} m^{-2} s^{-1}, and the WCA below 20° was observed after treating the samples in the afterglow for 0.05–0.5 s; corresponding O-atom doses 10^{22}–10^{23} m^{-2}. Larger doses caused a gradual loss of hydrophilicity, and an initial WCA of ~75° was established after treating the samples in the afterglow for ~40 s. This was attributed to the segregation and oxidation of iron on the NdFeB surface. Thorough XPS depth profiling revealed oxidation kinetics. The treatment in the glowing plasma caused a similar evolution, except that hydrophobicity was re-established after 1-s plasma treatment. The segregation of iron on the surface caused the formation of Fe_2O_3, and the intermediate layer toward the bulk consisted of Nd_2O_3 dispersed in the Fe matrix.

1. Introduction

Joining different materials with adhesive liquids is a standard technique for the synthesis of plastics with properties superior to bare polymers. The adhesive may be liquid at ambient conditions (such as glues before curing) or elevated temperatures (like molten polymers). The adhesion between the liquid and the solid material depends on various parameters, and the most important is wettability. The wettability stands for the ability of the liquid to penetrate pores, gaps, etc., between neighboring surfaces of the solid material. If the surface tension of the liquid is larger than the surface energy of the solid, the liquid will not interact with the entire surface of the solid material but only with segments stretching from the surface. This is known as the lotus leaf effect: a liquid droplet (water) slides from the tilted surface rather than wets it because of the highly hydrophobic surface. The hydrophobic surfaces are desired in many applications because they promote the self-cleaning effect, but are a drawback in other applications because they prevent adhesion or even mixing dispersion of a hydrophobic powder in liquids with moderately large polar component of the surface energy. The wettability could be increased by several techniques, and probably the most widely used is plasma treatment. The basic principle is explained in literature, and most authors report a severalfold increase in the adhesion force after plasma treatment [1].

Since the discovery of permanent magnets based on the grains of $Nd_2Fe_{14}B$ with a tetragonal crystalline structure [2,3], these materials have attracted significant attention from the scientific community due to their broad applications. Powdered magnetic materials can be sintered [4] or mixed with molten polymers to obtain bonded magnets [5]. An alternative approach for printing magnetic materials onto various substrates is the mixing of $Nd_2Fe_{14}B$ powders with liquid metals [6]. When magnetic powder is mixed with molten materials, the adhesion between magnetic grains is often inadequate [7]. The problem of poor adhesion remains an issue that has recently seen some novel solutions [8]. Poor wettability prevents optimal wetting of the magnetic powder with molten materials; therefore, the adhesion between the magnetic powder and the matrix is not adequate [9].

* Corresponding author.
E-mail address: gregor.primc@ijs.si (G. Primc).

https://doi.org/10.1016/j.apsusc.2025.164339
Received 13 May 2025; Received in revised form 11 August 2025; Accepted 12 August 2025
Available online 12 August 2025

The wettability of any material depends on its surface composition and structure, which are likely to deviate from that of the bulk material [10]. The magnetic flakes of commercial NdFeB magnets consist of $Nd_2Fe_{14}B$ grains with grain boundaries and triple joints between grains that are enriched in rare-earth compounds. Mazilkin et al. [11] reported the ratio between Nd and Fe in a typical grain boundary film of approximately 0.4, while the concentration of Fe in the triple joints between grains was below the detection limit. Electron energy loss spectroscopy (EELS) revealed that the concentration of metallic Nd in the triple junction was higher than that of Nd oxides. Similar results have been reported by Zhou et al. [12]. The high surface energy of commercial NdFeB magnets is likely the reason for the formation of quasi-periodic coarse-grained regions in hot-deformed NdFeB magnets, as recently shown by Chen et al. [13]. Uehara et al. [14] mentioned the possibility that the surface energy of Nd_2FeB grains depends on the crystallographic planes, while Hrkac et al. mentioned that the surface energy at the interface causes the rearrangement of the atoms close to the grain boundary [15].

The wettability of a solid material is often determined by measuring the contact angle formed after the deposition of a water droplet onto the surface of a solid material. The water droplet contact angle (WCA) indicates the macroscopic wettability, which is often a consequence of the surface structure and composition on a microscopic scale. This also depends on the morphology at the sub-micrometer scale. The surface of metallic samples is likely to be contaminated with organic impurities, which may dictate the WCA. The wettability is thus usually determined after cleaning the samples.

Xu et al. [16] measured the wettability of NdFeB magnets. The magnets were cut and polished with SiC papers of different grades from 100 to 1200. Next, they were ultrasonically cleaned in acetone and distilled water, dipped in a 5 % nitric acid solution for approximately 30 s at room temperature, and rinsed with distilled water. The polished and cleaned samples exhibited a WCA of 92°, indicating a moderately hydrophobic surface character.

Chen et al. studied the wettability of commercially available sintered NdFeB magnets [17]. The substrates were first degreased in 2.0 % NaOH solution for 120 s and then immersed in 5 % HNO_3 solution at room temperature for 90 s to remove rust. The samples were ultrasonically cleaned in acetone and rinsed with distilled water. The wettability was measured, and the WCA was approximately 45°. This value is significantly different from that reported by Xu et al. [16], and the reasons for this discrepancy cannot be evaluated because no additional data regarding the surface composition, structure, and morphology were provided.

The samples prepared by Chen et al. [17] were successfully hydrophilized by micro-arc oxidation. The treatment resulted in a superhydrophilic surface finish. Scanning electron microscopy (SEM) and energy-dispersive X-ray spectroscopy (EDX) revealed the formation of porous alumina on the magnet's surface, so the super-hydrophilic finish was due to the deposition of porous alumina film upon micro-arc oxidation rather than any modification of the surface properties of the NdFeB material. A hydrophobic coating was deposited after micro-arc oxidation, and the magnetic materials coated with porous alumina and a composite of poly(dimethylsiloxane) with embedded zinc oxide nanoparticles caused a superhydrophobic surface finish. The results reported by Chen et al. [17] clearly show that the wettability can be tailored by depositing either a porous hydrophilic coating (to obtain super-hydrophilicity) or a hydrophobic coating of rich morphology on the micrometer and nanometer scales (to obtain super-hydrophobicity).

Doping with low-melting-point metals improves the wettability of NdFeB magnets. Luo et al. [18] doped the magnetic material with Al, Sn, and Zn at a concentration well below 1 wt% and reported the formation of new alloys at grain boundaries. This phase promotes liquid-phase sintering to improve magnet density, wettability, and fluidity. Other methods for increasing the wettability of NdFeB materials include doping with nickel [19], lanthanum, yttrium [20], or gallium [21,22].

In this study, we investigated plasma treatment as a method for tailoring the wettability of magnetic powder to increase its adhesion to the molten polymer. Compared to the methods mentioned above, plasma allows easy manipulation of surface wettability and does not require additional rare-earth elements or coatings. Oxygen plasma is a source of radiation and reactive species such as positively charged ions, neutral atoms in the ground and excited states, and neutral molecules in metastable states, and the fluxes of these species onto a sample depend enormously on the discharge configuration, pressure, power, etc. We used two extreme cases: treatment in glowing plasma rich in all species, and in the flowing afterglow, where only long-living species are present. We used magnetic flakes rather than powder (the latter is usually used for the synthesis of bonded magnets) because the flakes enable hassle-free measurements of the wettability and surface and thin film composition.

2. Experimental details

2.1. Magnetic flakes

Commercially available NdFeB magnetic material was obtained from the Kolektor company (Idrija, Slovenia). They were in the form of flakes with a thickness of approximately 0.1 mm and an area of a few 10 mm^2. These flakes are used for further grinding to obtain the desired powder for the synthesis of the composite. The flakes are obtained by crushing the raw material synthesized by melt spinning a thin ribbon of the NdFeB alloy. The flakes are supposed to be free from lubricants or any other organics, and only the native oxide film should be on the surface. The flakes are visually smooth and their lateral dimension vary because of the crushing. The flakes with an almost rectangular shape and a lateral dimension of over 10 mm were selected for plasma treatments. Such a rather large surface of selected samples ensured that a deposited water droplet remained on the surface regardless of the wettability of the substrates.

Some plasma-treated samples were stored in the lab and probed for the wettability after different storage times ranging from.

2.2. X-ray photoelectron spectroscopy

The samples were characterized by X-ray photoelectron spectroscopy (XPS). An XPS instrument model PHI Genesis, from ULVAC-PHI (Physical Electronics Ltd., Munich, Germany), was used. The base pressure in the XPS analysis chamber was 5×10^{-7} Pa. The samples were excited with X-rays over a 100 μm^2 spot area with monochromatic Al $K\alpha_{1,2}$ radiation with a photon energy of 1486.6 eV. Photoelectrons were detected using a hemispherical analyzer positioned at an angle of 45° with respect to the normal of the sample's surface. Survey scan spectra were acquired at a pass energy of 280 eV and an energy step of 0.5 eV. High-resolution (HR) C 1s, O 1s, B 1s, Fe 2p, and Nd 3d spectra were acquired at a pass energy of 55 eV and 0.1 eV energy step. The measurement was on two different spots on the surface of each sample. The spectra were evaluated using the Multipak software (version 9.9.1.1) from Ulvac (Kanagawa, Japan). A Shirley-type background subtraction was used. The measured high-resolution XPS spectra were evaluated based on the binding-energy positions of the main peaks and characteristic satellite features.

XPS depth profiling of the samples was performed to remove the contaminated surface layer and determine the thickness of the oxide film formed during plasma treatment. Depth profiling was performed using an Ar^+ ion beam with the energy of 3 keV at an incidence angle of 45°, and a raster of 3 mm × 3 mm. This resulted in a sputtering rate of approximately 3 nm/min. A sputter rate of 3.0 nm/min was determined on the reference layer SiO_2 on Si, of a known thickness of 100 nm. The sputtering rate of the NdFeB material and thin films of oxides probably differ from that measured on SiO_2 due to different sputtering yields of elements and compounds, but the difference is expected to be lower than

30 %, which is the relative error for the determined depth scale in XPS depth profile.

During depth profiling, C 1s, O 1s, B 1s, Fe 2p, Nd 3d, and Nd 4d spectra were acquired at a pass energy of 140 eV and an energy step of 0.25 eV. The sputtering interval was set to 1 min. Because the Nd 3d peak overlapped with the O KLL Auger electron peak, an additional Nd 4d peak was measured as well to be able to calculate Nd concentration. The following sensitivity factors were used: C 1s (0.314), O 1s (0.733), B1s (0.171), Fe $2p_{3/2}$ (1.964), and Nd 4d (2.708). After depth profiling, the HR spectra of C 1s, O 1s, B 1s, Fe 2p, and Nd 3d were measured using the same parameters as before etching to reveal changes in the chemical state of these elements in more detail.

2.3. Water contact angle

Wettability was determined by measuring the contact angle of a water droplet deposited on the sample's surface. A Drop Analyzer DSA100E (KRUSS Scientific, Hamburg, Germany) was used, and the sessile drop method was employed. The surface was monitored with a camera during the deposition of the water droplet, and the WCA was determined. The volume of the water droplets was always 2 µl. Three repetitions of each measurement were performed to ensure the consistency of the results. The analyzer was in the same laboratory as the plasma reactor, so the time between the plasma treatment and the deposition of the water droplet was less than a minute. The ambient temperature in the laboratory was about 24 °C, and the relative humidity was about 70 %. All samples were visually very smooth (free from asperities), and a water droplet was deposited at the center of the flake to ensure it remained on the flake, even for most wettable surfaces where the water droplet spread significantly on the surface.

Samples with the highest wettability were stored in the laboratory and probed for hydrophobic recovery. A sample was placed into a covered Petri dish and removed from the dish occasionally to measure the water contact angle. The water was removed after measurement with a paper, and the sample was returned to the Petri dish. The temperature in the lab was between 23 and 26 °C and the relative humidity also varied during storage.

2.4. Atomic force microscopy

The surface morphology of the received NdFeB samples was measured using atomic force microscopy (AFM) with an NT-MDT instrument (Moscow, Russia). The measurements were performed in semi-contact mode using NT-MDT silicon tips. The AFM images were acquired over an area of 2 µm × 2 µm.

2.5. Plasma treatment

The NdFeB magnetic samples were exposed to oxygen plasma, which was sustained in the experimental system shown in Fig. 1. The magnetic samples were placed on a quartz glass holder, which was inserted into a long borosilicate glass tube with an inner diameter of 3.6 cm and a length of 80 cm. The system was pumped on one side using a two-stage rotary pump at a nominal pumping speed of 80 m^3/h to achieve an ultimate pressure of approximately 1 Pa. On the other side of the tube, oxygen with 99.999 %+ purity was introduced into the system via a precise needle valve. The pressure was measured using a capacitive absolute pressure gauge Baratron Pressure Transducer 722A (MKS, USA). Plasma was ignited using a CESAR Radiofrequency (RF) Power generator 1310 (Advanced Energy, USA) connected with a 6-turn water-cooled coil enveloping a part of the plasma tube. The RF generator operated at a frequency of 13.56 MHz and a power of 500 W, resulting in H-mode plasma inside the coil-covered volume. When 300 sccm of oxygen was introduced to the experimental system, the pressure was 50 Pa. The RF generator was controlled using a computer, allowing us to vary the power of the generator and discharge duration.

The samples were treated either in the glowing plasma inside the coil or in the oxygen plasma flowing afterglow, 20 cm away from the coil in the pumping direction, as shown in Fig. 1. The difference between the plasma and afterglow is in the concentration of various reactive oxygen species. In the plasma itself, the samples are subjected to both long- and short-lived species, whereas in the afterglow, only long-lived species are present. The short-lived species are charged particles (electrons, positively and negatively charged ions), metastables of high potential energy, and photons in the vacuum ultraviolet and visible ranges [23]. This causes the samples to heat up rapidly, as demonstrated in Fig. 2. A magnetic flake was connected to the thermocouple wires by spot welding and exposed either to the glowing plasma inside the coil or the

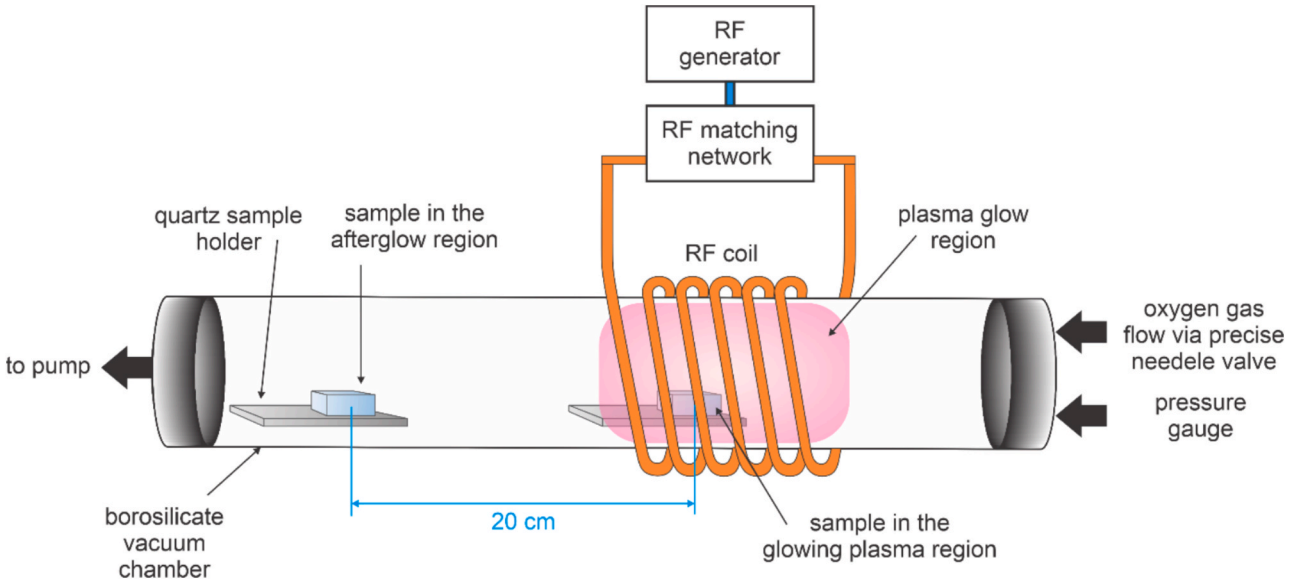

Fig. 1. Schematic of the experimental system. Plasma was ignited inside the RF coil, with O_2 entering the system at one end of the glass tube, passing through the coil (glow region) and towards the pump, passing through the afterglow region. The catalytic probe used to measure the density of neutral O atoms was placed at the exact same position as the sample in the afterglow region.

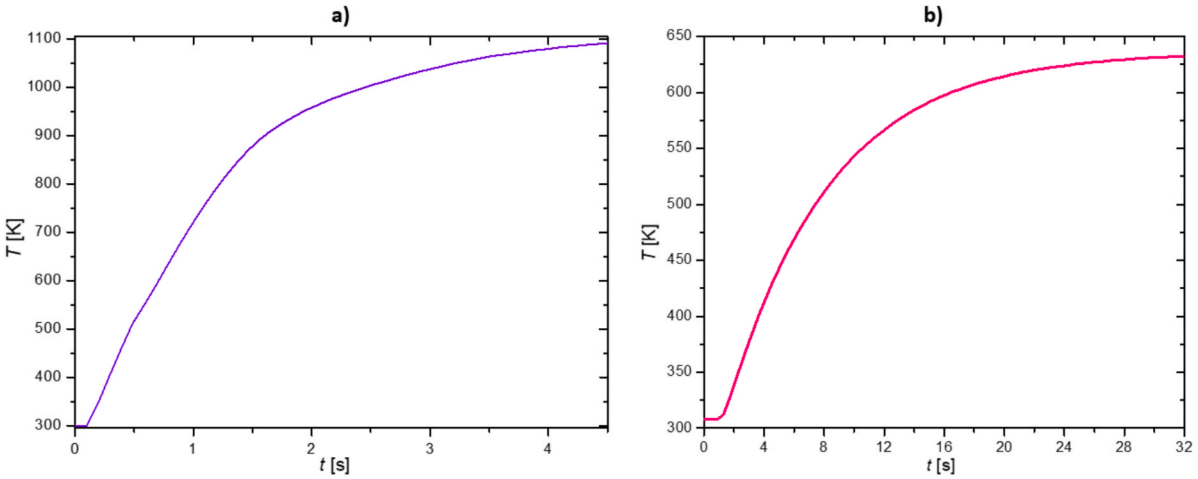

Fig. 2. Heating of magnetic samples in the glow (a) and afterglow (b) region of plasma.

flowing afterglow. The temperature of a sample placed into glowing plasma is shown in Fig. 2 (a). The discharge was turned on at a time of 0.15 s. The initial temperature rise is roughly 600 K/s. Some samples were mounted in the afterglow region, and the temperature is shown in Fig. 2 (b). The heating in the afterglow is not as pronounced as in the glow region, but the initial rise is at about 40 K/s. In both cases, the sample heats up to a certain point, after which the temperature remains fairly constant for the remainder of the plasma treatment. The predominant long-lived reactive plasma species in both the glowing plasma and the flowing afterglow are neutral oxygen atoms in the ground electronic state [24]. The concentration of O atoms in plasma and afterglow is similar and depends on the discharge parameters[25]. The density of the O atoms in the glowing plasma and afterglow was measured with a cobalt catalytic probe and was 5×10^{21} and 2×10^{21} m^{-3}, respectively.

3. Results and discussion

Several NdFeB samples were treated in the experimental system, as shown in Fig. 1. Systematic measurements were performed using WCA and XPS to reveal the evolution of the surface wettability as well as changes in the surface and thin film composition and structure.

3.1. AFM analysis of as-received magnetic flakes

AFM analyses were performed on the as-received NdFeB magnetic flakes to determine their surface morphology; a typical image is shown in Fig. 3. The samples were reasonably smooth with no distinct morphological features.

3.2. Wettability of the plasma-treated magnetic flakes

Several untreated samples were probed for wettability to determine variations between the samples. The untreated samples were hydrophobic and exhibited a WCA of between approximately 70° and 80°. The values were between those reported by Xu et al. [16] (92°) and Chen et al. [17] (45°). Both authors thoroughly cleaned the samples (degreasing and rust removal), and Xu et al. [16] also polished them. We measured the WCA of the as-received samples, i.e., without any polishing or cleaning. The reasons for the rather large differences between our results (70–80°), Xu et al. [16] (92°), and Chen et al. [17] (45°) are difficult to explain. This might be due to small differences in the manufacturing procedure. Unfortunately, the details are not available. In any case, the WCA was rather large, so the wettability of the as-received magnetic flakes was quite low.

Fig. 4 reveals the evolution of NdFeB wettability versus treatment time. The x-axis scale is logarithmic, which enables the visibility of wettability changes even for very short treatment times. Fig. 4a shows the evolution of the water contact angle for samples treated in the afterglow, and Fig. 4b for samples treated in glowing plasma. There are 2 x-axis scales in Fig. 4. The lower one is the treatment time, and the upper one is the fluence (dose) of neutral oxygen atoms.

For the samples treated with oxygen atoms in the flowing afterglow (Fig. 4a), the WCA initially decreased with the treatment time. Even a very short treatment time of 10 ms caused a significant decrease in WCA to approximately 30°. The error bar is rather large, which indicates that the hydrophilicity evolution is laterally inhomogeneous. Still, no outliers (values deviating unreasonably largely from the average value) were observed when measuring the water contact angles. Further treatment caused a gradual decrease in the WCA, and a minimum was

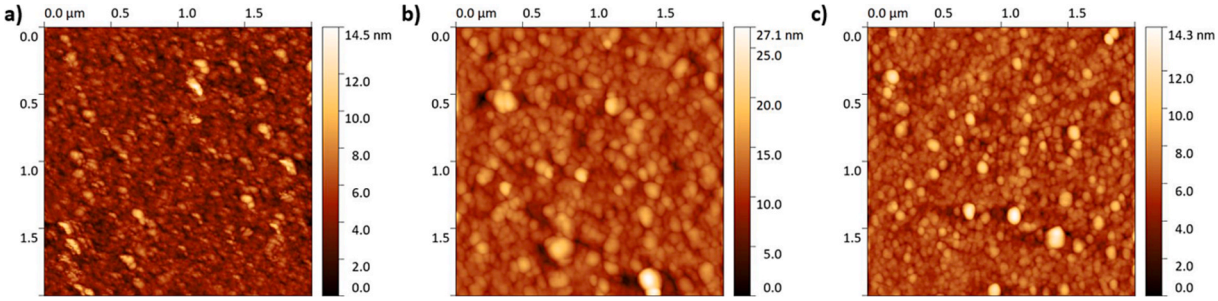

Fig. 3. An AFM image of the **(a)** as-received sample, **(b)** sample treated for 0.3 s in the afterglow, and **(c)** sample treated for 0.1 s in the glow region of plasma. The scanned area is 2 μm × 2 μm. Mean roughness R_a is 0.91 nm and RMS roughness R_q is 1.26 nm for the untreated sample, $R_a = 1.62$ nm and $R_q = 2.25$ nm for the sample treated in the afterglow, and $R_a = 0.87$ nm and $R_q = 1.22$ nm for the sample treated in the glow of plasma.

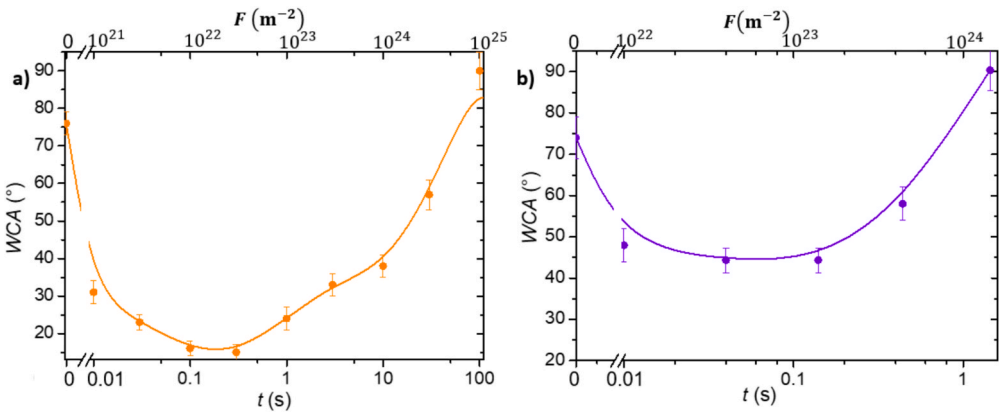

Fig. 4. Water contact angle (*WCA*) of samples treated in **(a)** O_2 flowing afterglow and **(b)** glowing plasma versus treatment time (*t*) and the fluence of oxygen atoms (*F*). In both cases, the pressure in the system was 50 Pa, and the forward power of the RF generator was 500 W. Fluence is calculated as the flux of atoms impinging on the sample multiplied by the exposure time. The symbols represent averaged measurements after selected treatment times, with the error bars representing the standard deviation.

observed (Fig. 4a) after approximately 0.3 s of treatment in the afterglow. The minimal WCA is below 20°, indicating a very wettable surface. Prolonged treatment times caused an increase in the WCA, and the surface returned to a hydrophobic state after treating the magnetic samples for several 10 s.

A similar wetting behavior, with the occurrence of a minimum, was also observed during the treatment of magnetic samples in the glowing plasma (Fig. 4b). The difference is that the minimum already occurs at a very short treatment time of the order of several 10 ms. The 10 ms treatment time (this is the minimal discharge duration supported by our RF generator) in the glowing oxygen plasma causes a significant drop in the WCA, and the error bars are rather large. For three identical samples, the WCA was either 62, 48, or 33° at the treatment time of 10 ms. The scattering of the measured values is usually explained by the small differences between virtually identical samples. In any case, the faster hydrophilization in Fig. 4b than in Fig. 4a can be explained by fluxes of various reactive oxygen species (ions, metastables, photons) to the sample's surface when exposed to the glowing plasma, in contrast to the flowing afterglow, where only oxygen atoms are present.

Another difference between Fig. 4 (a) and (b) is the wettability at the minimum. While the afterglow treatment enables the WCA below 20°, the treatment in the glowing plasma only enables WCAs down to about 45°, at least in the range of treatment times used in our experiments. Chemical analyses were performed to explain the appearance of a minimum in WCA and, thus, a maximum in surface wettability.

3.3. XPS analysis of the plasma-treated magnetic flakes

When exposed to oxygen plasma, a metallic sample is likely to be oxidized, even at low temperatures [26]. However, because every material contains a surface layer of impurities (i.e., adventitious carbon), the first effect of plasma is to clean the surface and remove organic impurities [27,28]. Typically, organic impurities are moderately hydrophobic [29]. Both the removal of the organic impurities and the formation of oxides are likely to influence the surface wettability. The oxidation kinetics were studied using XPS.

3.3.1. Modification of samples treated with oxygen plasma afterglow

The composition of the surface film of magnetic samples before and after treatment in oxygen plasma or its flowing afterglow was studied by XPS. XPS is a surface-sensitive technique that reveals the composition of the surface layer, the thickness of which is roughly the size of the escape depth of photoelectrons, that is, a few nanometers. Thicker films are characterized by depth profiling, i.e., acquiring XPS spectra after etching the surface film with energetic ions.

The surface compositions, calculated using the sensitivity factors, are listed in Table 1. The survey spectra were acquired on two measured points (spots) of each sample, so the numbers in Table 1 are average values over 2 spots. The theoretical values, taking into account the stoichiometric $Nd_2Fe_{14}B$ composition, are added to Table 1 (first row). A column indicating the ratio of iron to neodymium was added to the last column of Table 1. Oxygen and carbon prevailed in the XPS spectra acquired before the depth profiling of all samples. These elements are absent in stoichiometric materials; therefore, the surface is contaminated by impurities. The surface contamination with adventitious carbon is usually observed by XPS for most materials. The origin of such carbon is the adsorption of organic impurities from the air. A thorough study of the nature of such a contamination was performed by Gray et al. [30]. They identified about 20 organic molecules, including hydrocarbons, alcohols, ethers, ketones/aldehydes, and esters/acids, capable of adsorbing on the surfaces of solid materials. They also provided simulated adventitious C1s carbon spectra for various oxygen functionalities. In practice, the concentration of such adsorbed organic impurities varies, so it is not feasible to distinguish between all these adsorbed molecules.

Fig. 5 shows the XPS depth profiles of the untreated and afterglow-treated samples as a function of sputtering time. The depth profiles in Fig. 5 show carbon contamination only on the top of the samples, whereas oxygen persisted deeper in the investigated materials.

The untreated sample (Fig. 5a) contains a layer of native oxide. The oxygen concentration in the top surface layer, i.e., up to 2 min of sputtering with Ar^+ ions, was large, indicating complete oxidation of the metals in the uppermost surface film of the untreated samples. Beneath this very thin layer is another, thicker layer in which the oxygen content

Table 1
XPS surface compositions of $Nd_2Fe_{14}B$ samples.

Sample	C (at. %)	O (at. %)	Fe (at. %)	Nd (at. %)	B (at. %)	Fe/Nd
Theoretical			82.4	11.8	5.9	7.0
Untreated	26.7 ± 4.0	53.5 ± 1.2	5.9 ± 0.5	10.5 ± 0.7	3.6 ± 1.7	0.56
Afterglow 1 s	16.9 ± 7.5	59.7 ± 4.3	7.5 ± 2.1	12.4 ± 1.2	3.6 ± 1.8	0.61
Afterglow 5 s	12.7 ± 2.8	64.8 ± 2.0	17.9 ± 0.4	4.7 ± 0.3	0	3.8
Afterglow 30 s	14.9 ± 3.8	64.8 ± 2.1	18.7 ± 1.7	0.7 ± 0.6	0.8 ± 0.8	26.7
Glow 0.1 s	19.0 ± 1.3	56.7 ± 1.0	6.3 ± 0.8	14.7 ± 1.4	3.3 ± 1.7	0.43
Glow 1 s	18.9 ± 5.2	62.1 ± 4.5	17.5 ± 5.8	0.6 ± 0.6	0.9 ± 0.2	29.2

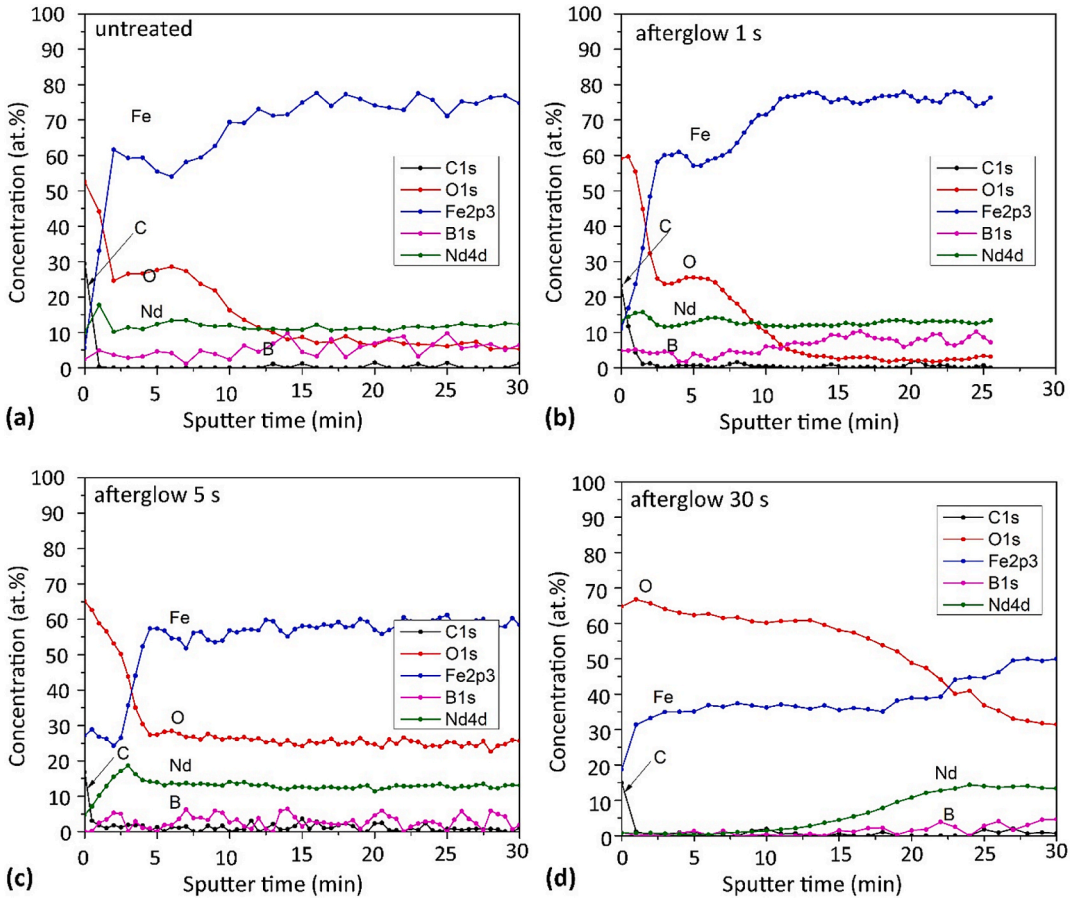

Fig. 5. XPS depth profiles of the **(a)** as-received samples, and samples treated in oxygen plasma afterglow **(b)** for 1 s, **(c)** for 5 s, and **(d)** for 30 s. The pressure was (50 Pa), and the discharge power was 500 W.

is only about half of the surface value. A thicker layer containing approximately 25–30 at.% oxygen (i.e., sputter times between 2 and about 7 min in Fig. 5a) could be attributed either to incomplete oxidation of metals in the film or to the artifact of the XPS depth profiling. Fig. 3 shows the morphological features that stretch up to approximately 10 nm from the average value. Such roughness is reflected in the preferential sputtering of bumps when Ar^+ ions are used for depth-profile etching. If the oxide film has a homogeneous thickness, the oxide film on the bumps is etched, but the oxide film in the valleys between the bumps persists. This effect is reflected in the broad interface in the XPS depth profiles. However, the depth profile in Fig. 5a does not reveal a broad interface with gradually decreasing oxygen concentration but rather a plateau between 2 and about 7 min of sputtering time. A gradual decrease in the oxygen concentration was only observed between sputtering times of 7 and 15 min. These rather unexpected results will be discussed below with reference to other depth profiles and high-resolution XPS spectra.

For the samples treated in the oxygen plasma afterglow, the thickness of the oxide layer (and oxygen concentration) depended on the treatment time. Fig. 5b shows the depth profile of a sample treated in oxygen plasma afterglow for 1 s. This treatment time resulted in a highly hydrophilic surface finish, as shown in Fig. 4a. The oxygen concentration on the very surface (Table 1) increases, and the carbon concentration decreases. The thickness of the oxide film on the sample treated in the afterglow for 1 s (Fig. 5b) was practically the same as that of the untreated sample (Fig. 5a). Therefore, the short treatment in the oxygen plasma afterglow causes significant hydrophilization of the magnetic material (Fig. 4a), but practically no oxidation as long as the thickness of the film containing 25–30 at.% oxygen is the merit. (Fig. 5b). Such a treatment time is therefore preferred if good surface wettability without oxidation is the priority. Namely, the WCA below 30° indicates good wettability. Still, one may speculate that the uppermost surface film with about 60 at.% oxygen is thicker after treatment in the afterglow for 1 s (Fig. 5a) than for an untreated sample (Fig. 5b).

Increasing the treatment time in the oxygen plasma afterglow resulted in the formation of thicker oxide films. Fig. 5c reveals a thick film with an oxygen concentration of approximately 25–30 % throughout the investigated depth, i.e., up to an ion sputtering time of 30 min, for the sample treated in oxygen plasma afterglow for 5 s. According to Fig. 4a, this treatment time already causes a loss of hydrophilicity because the WCA increases with increasing treatment time between 1 and 100 s. Fig. 5c reveals the segregation of Fe on the surface of the sample treated in the afterglow for 5 s, because the uppermost surface film contains little neodymium (Table 1). Below this iron-rich very thin surface film (after a sputtering time of 2 min), is a rather thick film with an almost perfectly constant composition. The oxygen concentration in this film (sputtering time between a few min and 30 min) is far below the value typical for fully oxidized metals. This observation suggests partial oxidation throughout the thick oxide film, which is explained below by referring to the high-resolution XPS spectra.

Surface segregation of iron is more obvious for longer treatment times. Fig. 5d shows the depth profile of a sample treated in afterglow for 30 s. Only iron and oxygen are observed up to the sputtering time of about 10 min. As shown in Fig. 5d, the concentration of oxygen is approximately 60 at.%, indicating the formation of Fe_2O_3. The oxygen concentration started to decrease when the concentration of Nd became measurable. Therefore, it can be concluded that prolonged treatment with oxygen-plasma afterglow causes the growth of a rather thick film of iron oxide on the surface of the NdFeB magnetic material. The whole

depth profile of the sample treated for 30 s (up to 150 min of sputtering) is shown in Supplemental (Fig. S1).

Such segregation of iron upon treatment with oxygen plasma or its afterglow has also been observed for other iron-containing alloys, such as stainless steel [31] and even Inconel (which contains a minor Fe concentration) [32]. The modification of the surface composition and structure led to significant changes in the surface wettability, as shown in Fig. 4a. Iron oxide is a hydrophobic material [33,34], so the growth of a rather thick film of this material on the surface may explain the monotonous increase in the WCA for prolonged treatment times in oxygen plasma afterglow.

3.3.2. *Modification of samples with glowing oxygen plasma*

As already mentioned, glowing oxygen plasma contains a considerable concentration of charged and metastable particles, and the surface reactions that lead to the neutralization of charged particles and relaxation of metastables are highly exothermic. Furthermore, the density of O atoms, which are likely to recombine on the surface and thus dissipate the dissociation energy, is more than twice as high as that in the afterglow, so the samples should heat up significantly in the glowing plasma. Therefore, the surface reactions that lead to the evolution of wettability should occur faster in the glowing plasma than in the afterglow. The evolution of the wettability, as shown in Fig. 4b, confirms this hypothesis. The minimal WCA was observed after about 0.1 s of treatment in the glowing plasma (Fig. 4b). On the other hand, the WCA at the minimum is larger than for samples treated in the afterglow. Taking into account the hydrophobic character of iron oxides [33], one may speculate that the formation of Fe_2O_3 film screens the beneficial effect, such as the removal of hydrophobic surface impurities.

The depth profiles of samples treated in the glowing plasma for 0.1 and 1 s are shown in Fig. 6a and 6b, respectively. The profile shown in Fig. 6a is almost identical to that shown in Fig. 5b. No significant oxidation was observed compared with the untreated sample (Fig. 5a). In fact, the oxygen concentration on the very surface (as determined from the XPS survey spectrum before sputtering with Ar ions) is even smaller than for the untreated sample (Table 1), but that might well be due to a localized deviation in the surface structure and composition. The depth profile shown in Fig. 6a corresponds to the minimum in the WCA (Fig. 4b), so it is possible to conclude again (as in Subsection 3.3.1) that the improved wettability is not attributed to the change in the surface composition of the magnetic material, but rather to the removal of the film of organic impurities (which are hydrophobic). The neodymium surface concentration (Table 1) remains rather large in the minima in WCA (Fig. 4), indicating little migration of Fe or B from the bulk NdFeB.

Fig. 6b shows the depth profile of a sample treated with a glowing oxygen plasma for 1 s. The surface film with a thickness corresponding to a sputtering time of 30 min contains only iron and oxygen, and the concentrations are constant, so it can be concluded that such treatment causes segregation of iron on the surface and its oxidation, so it is probably almost stoichiometric Fe_2O_3.

The depth profile of a sample treated in glowing plasma for 1 s up to 150 min of sputtering with Ar ions is shown in the Supplementary (Fig. S2). A similar composition was observed in Fig. 5d. There was a thick layer of Fe_2O_3 on the surface, followed by a layer containing O, Fe, Nd, and B, whereas the oxygen concentration in this layer was approximately 30 at.%. The thickness of the Fe_2O_3 film formed in the glowing plasma after treatment for 1 s was approximately 0.2 μm, as estimated from the sputtering rate (3 nm/min).

For all samples, the surface carbon contamination was reduced after only a minute of sputtering, which indicates that carbon was only present as adventitious carbon and not as an element from the bulk. Carbon might have adsorbed on the surface between the plasma treatment and the XPS characterization.

3.3.3. *Survey spectra for untreated and treated samples*

Fig. 7 shows the survey XPS spectra recorded on the surface before and after depth profiling of the samples. Peaks associated with Nd, Fe, B, C, and O are observed in the spectra before sputtering. The intensities of Fe and B were very low, whereas peaks C, O, and Nd predominated in the as-received sample (Fig. 7a). This observation is consistent with that of Mazilkin et al. [11], who reported triple joints between grains on the surface of magnetic materials, which are enriched in rare-earth compounds.

Significant changes can be observed after 30 min of sputtering of an untreated sample: the iron peak prevails as expected for stoichiometric $Nd_2Fe_{14}B$, the carbon peak disappears, and oxygen is present only in traces, indicating the removal of the surface layer of carbon and oxygen. In addition, small peaks related to niobium (Nb) appeared, but the intensity was close to the detection limit. Similar spectra were also observed for samples treated for 1 s in the afterglow (Fig. 7b), or 0.1 s in the glowing plasma (Fig. 7d). Prolonged plasma or afterglow treatment

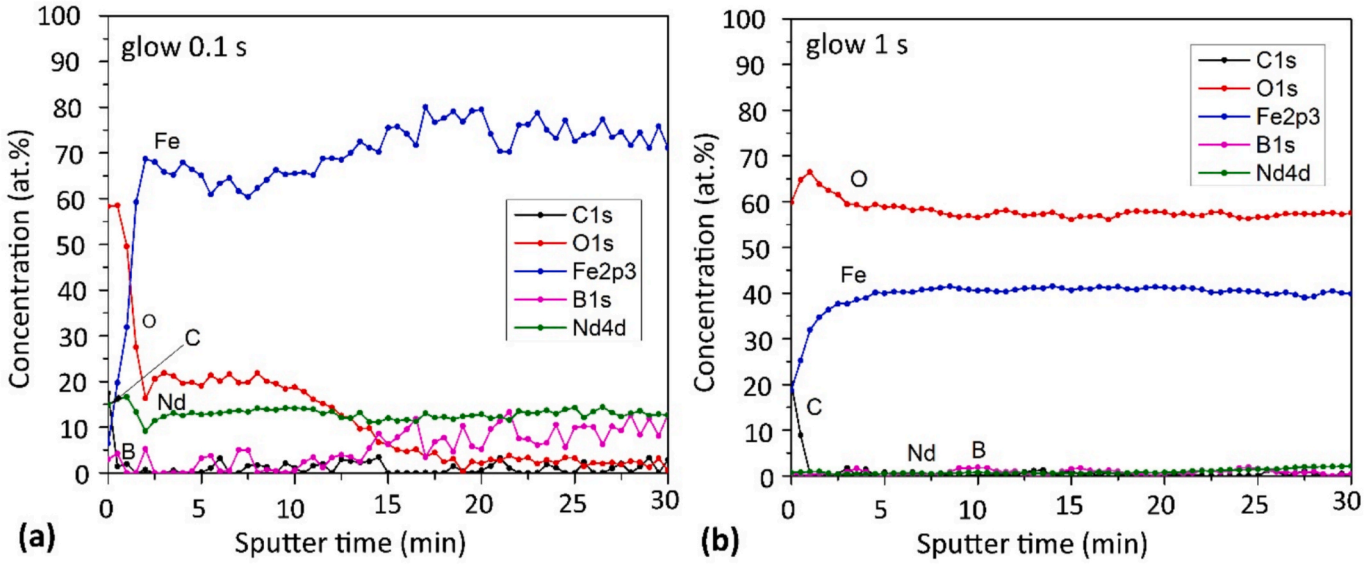

Fig. 6. XPS depth profiles of the samples treated in glowing oxygen plasma. **(a)** treated for 0.1 s, and **(b)** treated for 1 s. The pressure was (50 Pa) and the discharge power was 500 W.

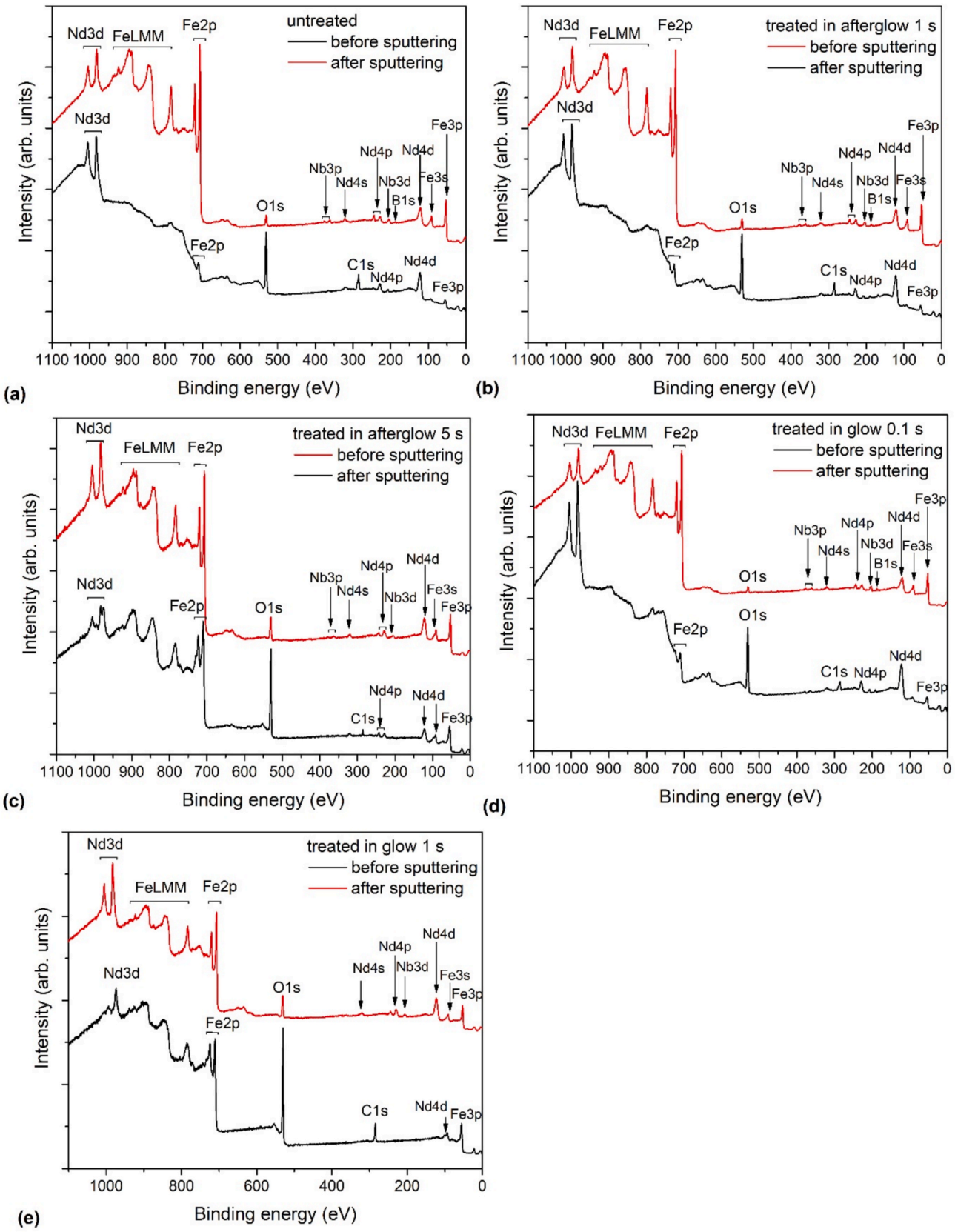

Fig. 7. XPS survey spectra before and after sputtering. **(a)** as-received, **(b)** treated in O_2 afterglow 1 s, **(c)** treated in O_2 afterglow 5 s, **(d)** treated in O_2 glow 0.1 s, and **(e)** treated in O_2 glow 1 s.

caused the persistence of an intensive oxygen peak also in spectra acquired after sputtering for 30 min (Fig. 7c and 7e, which is sound with the depth profiles shown in Figs. 5 and 6.

3.3.4. *Evolution of high-resolution spectra*

The survey spectra and the corresponding depth profiles enable the calculation of the composition, but do not reveal the oxidation states. The latter can only be deduced from the HR spectra of iron and neodymium. Figs. 8 and 9 show the HR spectra of Fe 2p and Nd 3d, respectively, for all treated samples. The set of curves in each figure was recorded after different sputtering times during depth profiling, with the bottom curve showing the initial spectrum before sputtering and the topmost curve showing the final spectrum after depth profiling. The parameter in these diagrams is the Ar^+ ion sputtering time.

The evolution of the HR-Fe spectra of the untreated sample is shown in Fig. 8a. The spectrum before sputtering (marked as 0 min) was significantly different from the other spectra because of the different surface compositions. The main peak of Fe $2p_{3/2}$ before sputtering is located at a binding energy of approximately 710.6 eV. This peak is related to iron from the native oxide layer (i.e., chemically bonded to oxygen or hydroxides; XPS does not distinguish between oxides and hydroxides). The presence of an additional satellite peak at 719 eV indicates that iron on the surface of an untreated sample was present in the Fe^{3+} oxidation state [35–37]. There is another small Fe $2p_{3/2}$ peak at 706.5 eV corresponding to bulk metallic iron Fe^0, which proves that the thickness of the native oxide layer is less than the detection depth of XPS, which is a few nanometers. This is consistent with the estimated oxide thickness in the depth profile shown in Fig. 5a. After removing the native layer of iron oxide, only the metal iron peak at 706.5 eV was observed in all spectra (except the bottom one), as shown in Fig. 8a.

The iron peak Fe^{3+} was also observed in the spectra acquired before Ar^+ ion sputtering for the samples treated with oxygen plasma afterglow or glowing plasma (Fig. 8b–f). This can be explained by the formation of the most stable iron oxide (Fe_2O_3) on the surface of the plasma-treated samples. For the samples treated for a short time (Fig. 8b, c, and e), the satellite peak at 719 eV quickly disappeared during depth profiling, even though the survey spectra (Figs. 5 and 6) showed a significant oxygen concentration.

The satellite peak at 719 eV persists in samples treated with larger doses of O atoms (treated in afterglow for 30 s – Fig. 8d, and treated in glowing plasma for 1 s – Fig. 8f). Those samples exhibited a thick oxide layer (Fig. 5d and Fig. 6b). The peak at 710.6 eV, belonging to the iron oxide, persists for quite a long time during Ar^+ ion sputtering and disappears only after prolonged sputtering time. It is worth mentioning that during the etching of iron oxide, a shift in the oxidation state of iron from Fe^{3+} toward a lower oxidation state (Fe^{2+}) is observed, which can be explained as a consequence of etching. This effect was well studied and reported in the literature for various metal oxides as well as for iron oxides, where it was found that preferential sputtering of oxygen leads to chemical reduction of iron oxides [38–40]. Moreover, as the intensity of the Fe oxide peak in Fig. 8 decreased, the peak corresponding to the Fe metal (at 706.5 eV) increased, indicating the presence of metallic iron below the surface layer enriched with iron oxide.

Here, an important observation should be noted. When the Fe $2p_{3/2}$ peak belonging to iron oxide disappears in the HR spectra shown in Fig. 8, oxygen is still present in the depth profiles shown in Figs. 5 and 6. This paradox can only be explained by considering that the oxygen in the subsurface film (where its concentration is 25–30 at.%) is not bound to iron but must be bound to neodymium (as shown in Fig. 9).

In contrast to iron, where the iron oxide peak quickly diminishes and transforms into pure iron metal, the HR neodymium spectra exhibit different behaviors. For the untreated sample (Fig. 9a), the Nd $3d_{5/2}$ peak is shifted during the sputtering from 982.6 ± 0.2 eV, which is according to the literature (see Table 2) characteristic of neodymium oxide in the Nd^{3+} state, to 980.8 ± 0.2 eV, which is characteristic of the metal Nd^0. Also, the shape of the peak is changed. The peak belonging to Nd oxide is highly asymmetric on its right side due to the overlap with the oxygen O KLL peak, whereas this is not observed for the Nd metal peak.

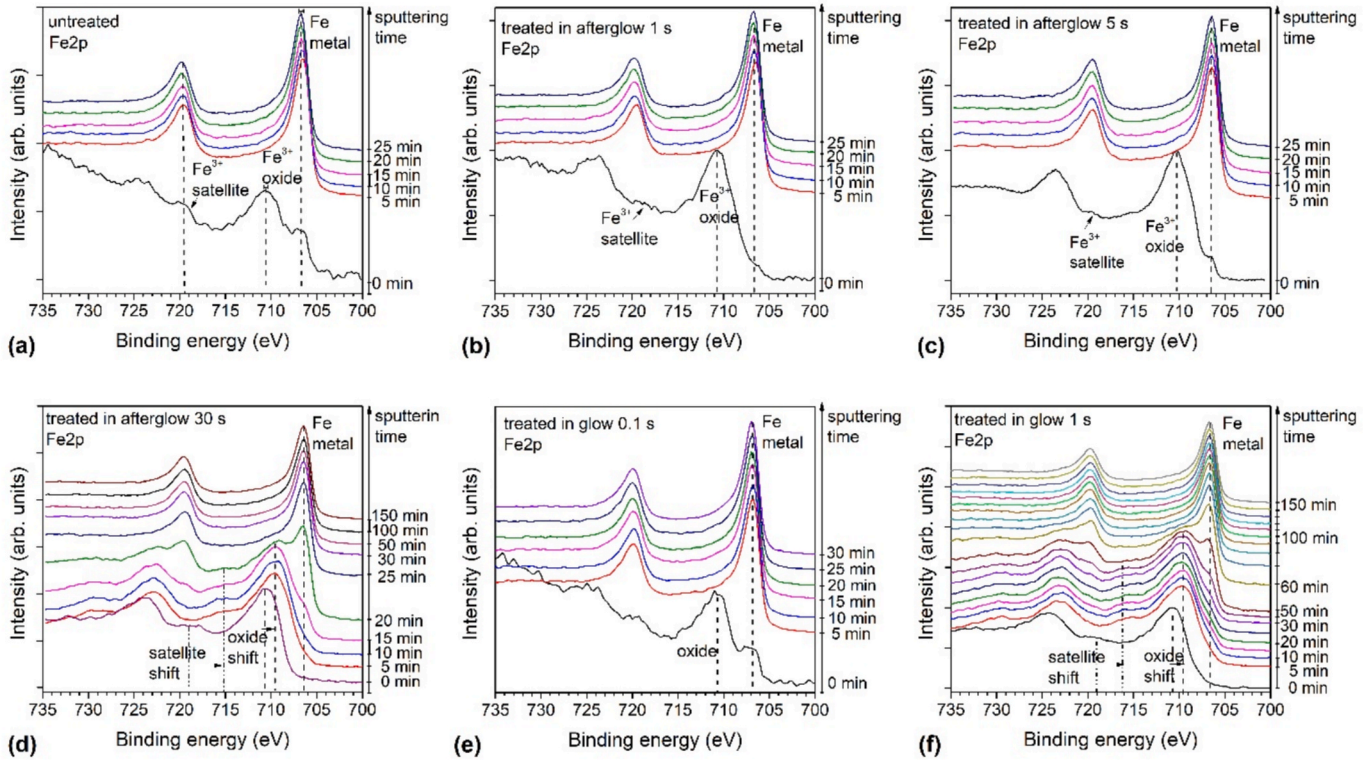

Fig. 8. Evolution of HR spectra of Fe 2p for: **(a)** the untreated sample, **(b)** the sample treated in the afterglow for 1 s, **(c)** the sample treated in the afterglow for 5 s, **(d)** the sample treated in the afterglow for 30 s, **(e)** the sample treated in the glow for 0.1 s, and **(f)** the sample treated in the glow for 1 s.

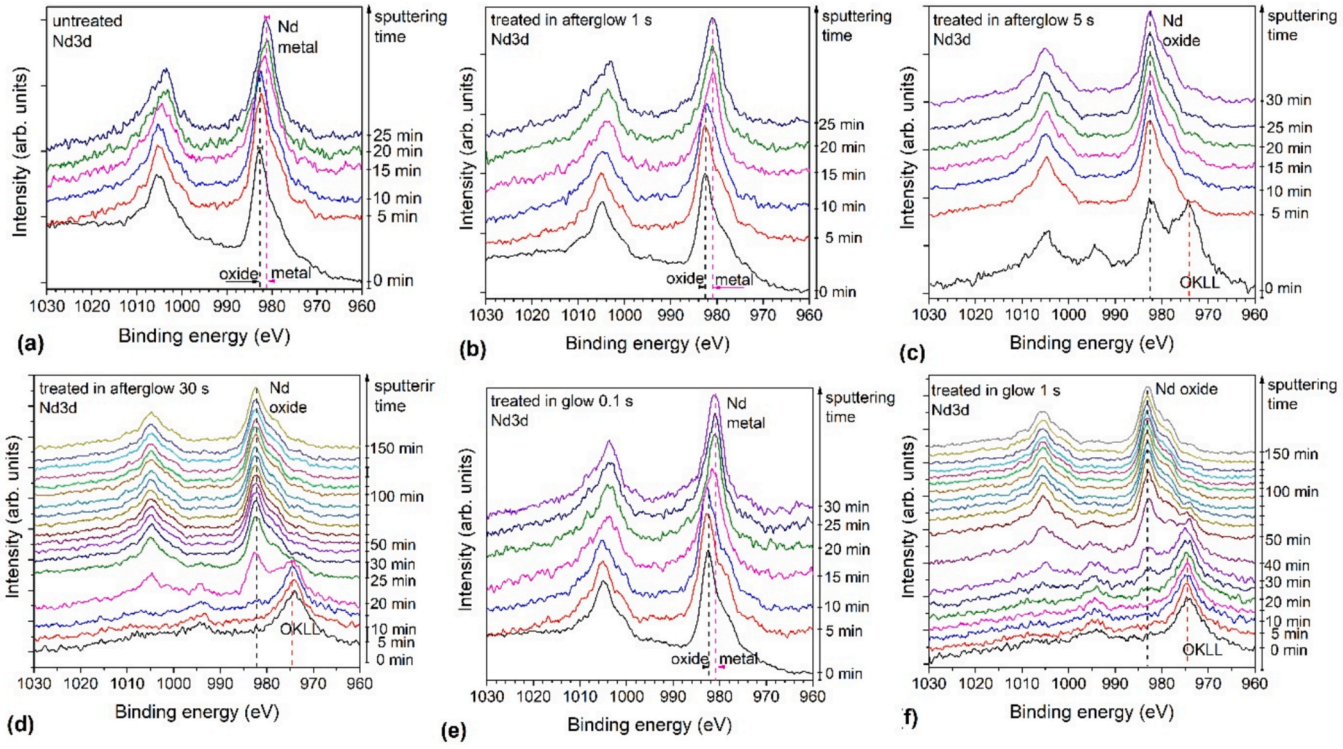

Fig. 9. Evolution of HR spectra of Nd 3d for: **(a)** the untreated sample, **(b)** the sample treated in the afterglow for 1 s, **(c)** the sample treated in the afterglow for 5 s, **(d)** the sample treated in the afterglow for 30 s, **(e)** the sample treated in the glow for 0.1 s, and **(f)** the sample treated in the glow for 1 s.

Table 2
Binding energies of the Nd $3d_{5/2}$ peak as reported in the literature.

	Binding energy of Nd $3d_{5/2}$	Reference
Nd metal	980.7 eV–980.9 eV	[41]
Nd metal/Cu	981.6 eV	[42]
Nd metal	980.5–981 eV	[42]
Nd_2O_3	981.7–982.3 eV	[42]
Nd_2O_3	982.2 eV	[43]
Nd_2O_3	983.1 eV	[44]
Nd_2O_3	981.7 eV	[45]
Nd_2O_3	983 eV	[46]
Nd metal	980.8 eV	our study
Nd_2O_3	982.6 eV	our study

The untreated sample thus has a thin Nd oxide layer just on the surface, as expected. Unlike the HR Fe spectra for the untreated sample (Fig. 8a), the Nd^{3+} component persists in Fig. 9a up to a sputtering time of approximately 10 min. The oxide film on the surface of the untreated sample shown in Fig. 5a (depth profile up to a sputtering time of 10 min) is thus attributed to niobium oxide. This is reasonable because the absolute value of the enthalpy of formation is much larger for neodymium than for iron oxide.

A similar shift of Nd from its oxide state to Nd metal was also observed for the samples treated for a short time (Fig. 9b and e). However, for the samples treated for a long time (Fig. 9c, d, f), the position of the Nd peak did not change; therefore, Nd remained oxidized throughout the entire etched layer, which was not observed for Fe (Fig. 8). Films containing 25–30 at.% oxygen in Figs. 5 and 6, therefore, consist of oxidized neodymium in metallic iron.

The wettability, as observed in Fig. 4, can be explained as follows: the untreated samples were moderately hydrophobic because of the presence of adsorbed impurities. These impurities were quickly removed by treatment with oxidizing species in the oxygen plasma or its flowing afterglow. The polar component of the surface energy of neodymium oxide is rather large; therefore, the minimum water contact angle in Fig. 4 is explained by the removal of surface impurities. Once the surface film of iron oxide starts forming, the wettability starts decreasing (WCA increases) until a hydrophobic surface finish typical for almost pure iron oxide is established.

Interestingly enough, the WCA keeps increasing with increasing treatment times despite the fact that the (almost complete) surface coverage with iron oxide (probably Fe_2O_3) has been observed already after 1 s of treatment in the glowing plasma or a few s in the flowing afterglow. Obviously, the wettability of our samples does not depend only on the surface composition. The wettability may also depend on the thickness of the iron oxide film in analogy to some other thin films [47]. Recently, the orientation of active surface sites on the hematite surface was found to influence the wettability significantly [48]. The detailed explanation of the effect observed in Fig. 4 is, thus, yet to be formulated.

Here, we should also note that overlapping Nd with O KLL causes complications in interpreting the XPS spectra when the oxygen concentration is high. Because the samples treated for a long time had a thick iron oxide layer on the surface and a very low Nd concentration, the O KLL peak from iron oxide prevailed directly on the surface (e.g., the black curve in Fig. 9d, f). However, when iron oxide vanished, which led to a decrease in the oxygen concentration, the Nd peak became clearly visible. Its position is still at 982.8 eV, corresponding to the Nd^{3+} oxide, whereas there are no signs of a shift to lower binding energies typical for Nd metal. A detailed analysis and interpretation of the XPS spectra indicate that the treatment of NdFeB materials with reactive species from oxygen plasma or its flowing afterglow causes surface segregation and oxidation of iron, and beneath is a layer of oxidized neodymium in the matrix of metallic iron.

Additionally, the hydrophobic recovery of the samples was studied. It is an inescapable reality for highly wettable materials because a large polar component of the surface energy is thermodynamically unfavorable. The best treatment parameters were selected to study the hydrophobic recovery. A sample treated in the oxygen plasma afterglow for 0.3 s exhibited a WCA of around 16°, measured immediately after the treatment (Fig. 4a). The evolution of WCA upon storage at ambient

conditions for this sample is shown in Fig. 10. The hydrophobic recovery is moderate, because the WCA around 45° was determined after storing the treated sample at ambient conditions for two hours (increase of 250 %). This WCA is still less than the WCA for the untreated sample (about 75°, Fig. 4), so the increased wettability persists for several hours after treating the samples in oxygen plasma. Fig. 10 reveals that the hydrophobic recovery follows a fairly linear behavior in the lin-log scale, so the increase is logarithmic.

Here, it is worth mentioning that the hydrophobic recovery may not be an obstacle in any industrial application because the plasma-treated material is supposed to be used for the synthesis of composites soon after the plasma treatment. Preferably, the plasma-treated magnetic and polymer powder are mixed, and the composite is synthesized by extrusion.

4. Conclusions

Reactive species from oxygen plasma enabled rapid hydrophilization of NdFeB materials without any precleaning or other treatments. Treatment in the oxygen plasma afterglow resulted in a water contact angle of approximately 20°, which is typical for highly hydrophilic materials. The range of doses of O atoms useful for optimal hydrophilization by treatment in the afterglow is between about 0.5 and 30 × 10^{22} m^{-2}, preferably between 1 and 6 × 10^{22} m^{-2}. This range of doses enabled surface activation and did not cause significant diffusion of Fe on the surface, where it was transformed into hydrophobic Fe_2O_3. Hydrophilization is not as effective upon exposure of NdFeB materials to glowing oxygen plasma because the minimal achievable WCA is between 40 and 50°. The glowing oxygen plasma causes significant heating of NdFeB materials, which stimulates the diffusion of Fe onto the surface. The recommended dose of O atoms when using direct treatment in the glowing plasma is up to 1 × 10^{23} m^{-2}. Larger doses should be avoided because they stimulate the diffusion of iron onto the surface as well as oxygen toward the bulk material, and the latter effect causes the formation of an intermediate film rich in metallic iron and oxidized neodymium. The formation of the thick oxide film will probably suppress the magnetic properties so large doses of O atoms should be avoided at any practical application.

The recommended doses are achievable in low-pressure reactors in a reasonable time (around a second), provided the O-atom density is large enough. The density depends enormously on the discharge parameters, including the power density and the type of material the reactor is made from. O-atom densities of the order of 10^{20} are achieved in an industrial-size low-pressure reactor at a power density as low as about 10 W/litre, provided the reactor is made from (or coated with) a material which exhibits a low coefficient for the surface recombination, such as smooth glasses or ceramics. However, a user should be aware of the gradients in the O-atom density next to the magnetic material because it represents a sink for O-atoms. The requirement for a vacuum system will add to the costs of the production line, but it is unavoidable wherever numerous objects with a complex geometry are to be uniformly treated with gaseous plasma.

In our experimental systems, the samples were always kept at the floating potential, so the kinetic energy of ions is not large. In the collisionless-sheath approximation, the positively charged ions bombard the surface of the samples perpendicularly with the kinetic energy, which corresponds to the voltage drop between the plasma and floating potential, which should roughly be about 10 V.

CRediT authorship contribution statement

Domen Paul: Writing – original draft, Methodology, Conceptualization. **Alenka Vesel:** Writing – review & editing, Validation, Resources, Project administration, Methodology. **Miran Mozetič:** Writing – review & editing, Writing – original draft, Supervision, Project administration, Funding acquisition, Data curation, Conceptualization.

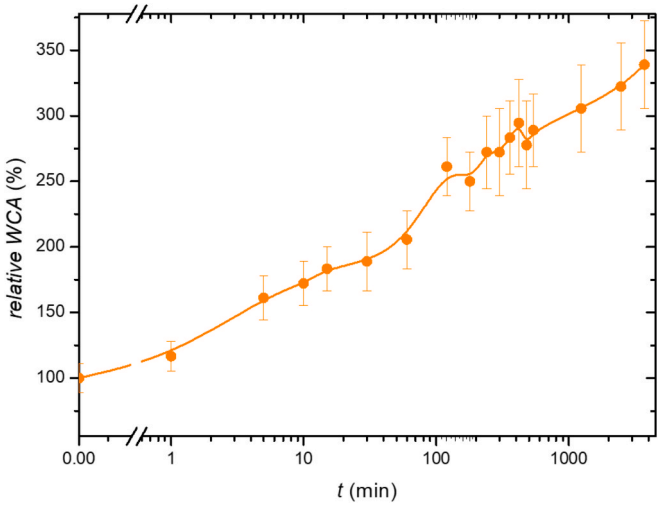

Fig. 10. Hydrophobic recovery of samples treated for 0.3 s in the afterglow of H-mode oxygen plasma – relative water contact angle (*relative WCA*) versus elapsed time (*t*) after plasma treatment. The relative WCA was calculated concerning the initial value immediately after plasma treatment.

Rok Zaplotnik: Writing – review & editing, Visualization, Validation, Supervision, Data curation. **Marian Lehocky:** Resources, Formal analysis. **Nataša Kovačević:** Validation, Investigation. **Gregor Primc:** Writing – review & editing, Visualization, Validation, Methodology.

Declaration of competing interest

The authors declare the following financial interests/personal relationships which may be considered as potential competing interests: Domen Paul, Alenka Vesel, Miran Mozetic, Rok Zaplotnik reports financial support was provided by Slovenian Research and Innovation Agency. Gregor Primc reports financial support was provided by Slovenian Research and Innovation Agency. If there are other authors, they declare that they have no known competing financial interests or personal relationships that could have appeared to influence the work reported in this paper.

Acknowledgments

This research was funded by the Slovenian Research Agency, Core Funding No. P2-0082 (Thin Film Structures and Plasma Surface Engineering) and Project No. L1-50007 (Non-equilibrium Plasma Processing for Superior Composite Magnets). The authors gratefully acknowledge Dr. D. Lojen and J. Trtnik for technical assistance and AFM measurements.

Appendix A. Supplementary data

Supplementary data to this article can be found online at https://doi.org/10.1016/j.apsusc.2025.164339.

Data availability

The data supporting the findings of this study are available in Zenodo at DOI: 10.5281/zenodo.15045365.

References

[1] G. Primc, M. Mozetič, Surface modification of polymers by plasma treatment for appropriate adhesion of coatings, Materials 17 (2024) 1494, https://doi.org/10.3390/ma17071494.

[2] M. Sagawa, S. Fujimura, N. Togawa, H. Yamamoto, Y. Matsuura, New material for permanent magnets on a base of Nd and Fe, J. Appl. Phys. 55 (1984) 2083, https://doi.org/10.1063/1.333572.

[3] J.J. Croat, J.F. Herbst, R.W. Lee, F.E. Pinkerton, Pr-Fe and Nd-Fe-based materials: a new class of high-performance permanent magnets, J. Appl. Phys. 55 (1984) 2078, https://doi.org/10.1063/1.333571.

[4] Y. Luo, N. Zhang, C.D. Graham Jr., Variation of hardness with temperature in sintered NdFeB magnets, J. Appl. Phys. 61 (1987) 3442, https://doi.org/10.1063/1.338747.

[5] A.Z. Liu, I.Z. Rahman, M.A. Rahman, E.R. Petty, Fabrication and measurements on polymer bonded NdFeB magnets, J. Mater. Process. Technol. 56 (1996) 571, https://doi.org/10.1016/0924-0136(95)01871-9.

[6] Z. Zhu, R. Zhao, B. Ye, H. Wang, Liquid-metal/NdFeB/Ni composites for high wettability, patternable, stretchable electronic wire, AIP Adv. 13 (2023), https://doi.org/10.1063/5.0158221.

[7] L. Li, K. Jones, B. Sales, J.L. Pries, I.C. Nlebedim, K. Jin, H. Bei, B.K. Post, M. S. Kesler, O. Rios, V. Kunc, R. Fredette, J. Ormerod, A. Williams, T.A. Lograsso, M. P. Paranthaman, Fabrication of highly dense isotropic Nd-Fe-B nylon bonded magnets via extrusion-based additive manufacturing, Addit. Manuf. 21 (2018) 495, https://doi.org/10.1016/j.addma.2018.04.001.

[8] G. Primc, M. Mozetič, Recent advances in corrosion inhibition of bonded NdFeB magnets, Materials 17 (2024) 2475, https://doi.org/10.3390/ma17112475.

[9] A. Damnjanović, G. Primc, R. Zaplotnik, M. Mozetič, N. Kovačević, The impact of plasma surface treatments on the mechanical properties and magnetic performance of FDM-printed NdFeB/PA12 magnets, Materials 17 (2024) 2275, https://doi.org/10.3390/ma17102275.

[10] Z. Wang, G. Wang, Y.-F. Li, H. Cao, Z.-M. Huo, B.-Z. Xin, W.-J. Li, Y. Yu, Y. Wang, Z. Lu, Wettability transition methods for metal surface after laser processing, Opt. Laser Technol. 191 (2025) 113406, https://doi.org/10.1016/j.optlastec.2025.113406.

[11] A. Mazilkin, B.B. Straumal, S.G. Protasova, S. Gorji, A.B. Straumal, M. Katter, G. Schütz, B. Barezky, Grain boundary oxide layers in NdFeB-based permanent magnets, Mater. Des. 199 (2021) 109417, https://doi.org/10.1016/j.matdes.2020.109417.

[12] Q. Zhou, W. Li, Y. Hong, L. Zhao, X. Zhong, H. Yu, L. Huang, Z. Liu, Microstructure improvement related coercivity enhancement for sintered NdFeB magnets after optimized additional heat treatment, J. Rare Earths 36 (2018) 379, https://doi.org/10.1016/j.jre.2017.11.007.

[13] H. Chen, R. Wang, J. Li, C. Liu, X. Zhang, Y. Liu, Origin of the quasi-periodic coarse grain regions in hot-deformed Nd-Fe-B magnets, Mater Charact 204 (2023) 113238, https://doi.org/10.1016/j.matchar.2023.113238.

[14] M. Uehara, N. Gennai, M. Fujiwara, T. Tanaka, Improved perpendicular anisotropy and permanent magnet properties in Co-doped Nd-Fe-B films multilayered with Ta, 2005 IEEE International Magnetics Conference (INTERMAG), Nagoya, Japan, 4-8 April, 2005, p. 931, DOI: 10.1109/INTMAG.2005.1463894.

[15] G. Hrkac, K. Butler, T.G. Woodcock, L. Saharan, T. Schrefl, O. Gutfleisch, Modeling of Nd-oxide grain boundary phases in Nd-Fe-B sintered magnets, JOM 66 (2014) 1138, https://doi.org/10.1007/s11837-014-0980-5.

[16] J.L. Xu, Z.C. Zhong, Z.X. Huang, J.M. Luo, Corrosion resistance of the titania particles enhanced acrylic resin composite coatings on sintered NdFeB permanent magnets, J. Alloys Compd. 570 (2013) 28, https://doi.org/10.1016/j.jallcom.2013.03.033.

[17] J. Chen, J.L. Xu, J. Huang, L. Dai, M.S. Xue, J.M. Luo, Corrosion resistance of T-ZnOw/PDMS-MAO composite coating on the sintered NdFeB magnet, J. Magn. Magn. Mater. 534 (2021) 168049, https://doi.org/10.1016/j.jmmm.2021.168049.

[18] S. Luo, Y. Lu, Y. Zou, S. Zhong, Y. Wu, M. Yang, Effect of low melting point powder doping on the properties and microstructure of sintered NdFeB magnets, J. Magn. Magn. Mater. 523 (2021) 167620, https://doi.org/10.1016/j.jmmm.2020.167620.

[19] P. Zhang, L. Liang, J. Jin, Y. Zhang, X. Liu, M. Yan, Magnetic properties and corrosion resistance of Nd–Fe–B magnets with Nd64Co36 intergranular addition, J. Alloys Compd. 616 (2014) 345, https://doi.org/10.1016/j.jallcom.2014.07.085.

[20] C. Zhao, Q. Jiang, S.U. Rehman, X. Li, Y. Chen, J. Song, Z. Zhong, Effect of La–Y co-substitution on magnetic properties and microstructure of NdFeB alloy ribbons, J. Rare Earths 2022 (1894) 40, https://doi.org/10.1016/j.jre.2021.11.011.

[21] X.D. Xu, T.T. Sasaki, J.N. Li, Z.J. Dong, H. Sepehri-Amin, T.H. Kim, T. Ohkubo, T. Schrefl, K. Hono, Microstructure of a Dy-free Nd-Fe-B sintered magnet with 2 T coercivity, Acta Mater. 156 (2018) 146, https://doi.org/10.1016/j.actamat.2018.06.037.

[22] M. Yan, W. Chen, J. Jin, Y. Liu, H. Chen, S.P. Ringer, J. Xu, Y. Hou, M. Yue, X. Liu, Merits of Pr80Ga20 grain boundary diffusion process towards high coercivity–remanence synergy of Nd–La–Ce–Fe–B sintered magnet, Acta Mater. 231 (2022) 117873, https://doi.org/10.1016/j.actamat.2022.117873.

[23] M. Mozetic, Extremely non-equilibrium oxygen plasma for direct synthesis of metal oxide nanowires on metallic substrates, J. Appl. Phys. D Appl. Phys. 44 (2011) 174028, https://doi.org/10.1088/0022-3727/44/17/174028.

[24] J.-P. Booth, M. Mozetič, A. Nikiforov, C. Oehr, Foundations of plasma surface functionalization of polymers for industrial and biological applications, Plasma Sources Sci. Technol. 31 (2022) 103001, https://doi.org/10.1088/1361-6595/ac70f9.

[25] R. Zaplotnik, G. Primc, D. Paul, M. Mozetič, J. Kovač, A. Vesel, Atomic specie generation by plasmas, in: Plasma Applications for Material Modification: from Microelectronics to Biological Materials, Jenny Stanford Publishing, Singapore, 2021, p. 107.

[26] T. Saburi, T. Suzuki, K. Kiuchi, Y. Fujii, Reaction rates of refractory metal oxidation in cold oxygen plasma, Thin Solid Films 506–507 (2006) 331, https://doi.org/10.1016/j.tsf.2005.08.077.

[27] P. Krüger, R. Knes, J. Friedrich, Surface cleaning by plasma-enhanced desorption of contaminants (PEDC), Surf. Coat. Technol. 112 (1999) 240, https://doi.org/10.1016/S0257-8972(98)00777-4.

[28] C.-S. Park, S.-K. Jang, H.-S. Tae, E.-Y. Jung, Effects of RF-plasma pretreatment on panel-aging characteristics in AC plasma display panel with full-HD cell size, Mol. Cryst. Liq. Cryst. 551 (2011) 95, https://doi.org/10.1080/15421406.2011.600161.

[29] N. Nioradze, R. Chen, N. Kurapati, A. Khvataeva-Domanov, S. Mabic, S. Amemiya, Organic contamination of highly oriented pyrolytic graphite as studied by scanning electrochemical microscopy, Anal. Chem. 87 (2015) 4836, https://doi.org/10.1021/acs.analchem.5b00213.

[30] L.H. Grey, H.-Y. Nie, M.C. Biesinger, Defining the nature of adventitious carbon and improving its merit as a charge correction reference for XPS, Appl. Surf. Sci. 653 (2024) 159319, https://doi.org/10.1016/j.apsusc.2024.159319.

[31] A. Vesel, M. Mozetič, A. Zalar, Oxidation of AISI 304L stainless steel surface with atomic oxygen, Appl. Surf. Sci. 200 (2002) 94, https://doi.org/10.1016/S0169-4332(02)00647-5.

[32] A. Vesel, A. Drenik, K. Elersic, M. Mozetic, J. Kovac, T. Gyergyek, J. Stockel, J. Varju, R. Panek, M. Balat-Pichelin, Oxidation of Inconel 625 superalloy upon treatment with oxygen or hydrogen plasma at high temperature, Appl. Surf. Sci. 305 (2014) 674, https://doi.org/10.1016/j.apsusc.2014.03.160.

[33] S. He, J. Shi, J. Huang, J. Hu, Y. Lai, Z. Chen, Rational designed structured superhydrophobic iron oxide surface towards sustainable anti-corrosion and self-cleaning, Chem. Eng. J. 416 (2021) 127768, https://doi.org/10.1016/j.cej.2020.127768.

[34] T. Maeda, C. Fukumoto, T. Matsumura, K. Nisioka, M. Shimizu, Effect of adding moisture and wettability on granulation of iron ore, Tetsu-to-Hagane 92 (2006) 721, https://doi.org/10.2355/tetsutohagane1955.92.12_721.

[35] T. Yamashita, P. Hayes, Analysis of XPS spectra of Fe^{2+} and Fe^{3+} ions in oxide materials, Appl. Surf. Sci. 254 (2008) 2441, https://doi.org/10.1016/j.apsusc.2007.09.063.

[36] A.P. Grosvenor, B.A. Kobe, M.C. Biesinger, N.S. McIntyre, Investigation of multiplet splitting of Fe 2p XPS spectra and bonding in iron compounds, Surf. Interface Anal. 36 (2004) 1564, https://doi.org/10.1002/sia.1984.

[37] T.-C. Lin, G. Seshadri, J.A. Kelber, A consistent method for quantitative XPS peak analysis of thin oxide films on clean polycrystalline iron surfaces, Appl. Surf. Sci. 119 (1997) 83, https://doi.org/10.1016/S0169-4332(97)00167-0.

[38] D.F. Mitchell, G.I. Sproule, M.J. Graham, Sputter reduction of oxides by ion bombardment during Auger depth profile analysis, Surf. Interface Anal. 15 (1990) 487, https://doi.org/10.1002/sia.740150808.

[39] M.F. Toney, S. Brennan, Structural depth profiling of iron oxide thin films using grazing incidence asymmetric Bragg x-ray diffraction, J. Appl. Phys. 65 (1989) 4763, https://doi.org/10.1063/1.343230.

[40] M. Fondell, M. Gorgoi, M. Boman, A. Lindblad, Surface modification of iron oxides by ion bombardment – Comparing depth profiling by HAXPES and Ar ion sputtering, J. Electron Spectrosc. Relat. Phenom. 224 (2018) 23, https://doi.org/10.1016/j.elspec.2017.09.008.

[41] The International XPS Database, XPS Metrology & Labs LLC, 2025, January 28, 2025, https://xpsdatabase.net/boron-b-z5-boron-compounds/.

[42] J.F. Moulder, W.F. Stickle, P.E. Sobol, K.D. Bomben, Handbook of X-ray Photoelectron Spectroscopy PHI, Chanhassen, Minnesota, 1995.

[43] S. Zhang, Y. Chang, A. Xu, J. Jia, M. Jia, Preparation of 3D Nd_2O_3-NiSe-modified nitrogen-doped carbon and its electrocatalytic oxidation of methanol and urea, Nanomaterials 13 (2023) 814.

[44] J.P. Baltrus, M.J. Keller, Rare earth oxides Eu_2O_3 and Nd_2O_3 analyzed by XPS, Surf. Sci. Spectra 26 (2019), https://doi.org/10.1116/1.5085768.

[45] S.H. Jeon, K. Nam, H.J. Yoon, Y.-I. Kim, D.W. Cho, Y. Sohn, Hydrothermal synthesis of Nd2O3 nanorods, Ceram. Int. 43 (2017) 1193, https://doi.org/10.1016/j.ceramint.2016.10.062.

[46] R. Yuvakkumar, S.I. Hong, Nd_2O_3: novel synthesis and characterization, J. Sol-Gel Sci. Technol. 73 (2015) 511, https://doi.org/10.1007/s10971-015-3629-0.

[47] J. Kaur, R.K. Jain, A. Khanna, A.K. Cawla, Effects of thickness on the wettability and electrical properties of Sn thin films, J. Vac. Sci. Technol. B 39 (2021) 032205, https://doi.org/10.1116/6.0001026.

[48] L.M. Faustino, B. McFadzean, J.T. Gouvea Junior, L. de Salles Leal Filho, Bulk and surface characterization of distinct hematite morphology: implications for wettability and flotation response, Minerals 14 (2024) 609, https://doi.org/10.3390/min14060609.